Check for updates

Batteries & Supercaps

Research Article
doi.org/10.1002/batt.202100350

Chemistry Europe
European Chemical Societies Publishing

www.batteries-supercaps.org

Biomass-Derived Hierarchically Porous (Nitrogen, Phosphorus) Co-Doped SiO_x/C Composite Nanosheet Architectures for Superior Lithium Storage and Ultra-Long Cycle Performance

Luting Song,[a] Tingqiao Zhao,[a, b] Xinghua Tan,[a, b] Dongdong Mao,[a, b] Sai Su,[a, b] Zhengwei Fan,[a, b] and Weiguo Chu*[a, b]

Biomasses receive much attention as carbon sources for anodes of high-energy lithium-ion batteries and cathodes of lithium-sulfur batteries due to their low costs, easy availability and potentially high capacities which unfortunately deliver unsatisfactory performances normally. However, biomasses used as silicon instead of carbon-dominated sources have never been touched before. Here, we report a facile preparation of nitrogen and phosphorus heteroatoms co-doped hierarchically porous and cross-linked SiO_x/C composite nanosheet architectures from catkins without the introduction of alien Si (N/P-SiO_x/C-NSs) using chemical exfoliation and treatments. This unique structure composed of novel multiple-phase composites is revealed to show superior fast kinetics and ultra-long cycle life with about 340 mAh g^{-1} and almost no capacity decay after 10000 cycles at 10 A g^{-1}, far beyond those of conventional carbon and SiO_x-based anode materials. The superior performance is closely related to excellent electronic conduction arising from the cross-linkage architecture, well-graphitized carbon and uniform co-doping of nitrogen and phosphorus, rapid ionic transport kinetics from rich hierarchical pores, and outstanding stability from the rigid nanosheet networks. This study sets a precedent of catkins as silicon instead of conventional carbon-only sources for anode materials, which can largely enhance the role of biomasses in energy storage.

Introduction

Lithium-ion batteries (LIBs) have been successfully commercialized to meet the demands of continually growing energy and global CO_2 emission reduction as indispensable energy storage devices because of long cycle stability, and high energy density and working potential.[1–3] As a result, both novel cathode[4] and anode materials such as carbon-,[5,6] silicon-,[7–9] and tin-based anode materials,[10] with high capacity, long-term stability and environmental friendliness are highly desired for next-generation power systems.[3,11–13]

Currently, conventional intercalation-type graphite anode materials are largely restricted by a low theoretical capacity (LiC_6: 372 mAh g^{-1}) and inferior rate performances and therefore difficult to satisfy the ever-increasing needs of energy storage though already commercialized.[6,14] Fortunately, the emergence of silicon-based anode nanomaterials brings about great promise for next-generation LIBs because of a high theoretical capacity ($Li_{15}Si_4$, 3579 mAh g^{-1}), abundance and low working potential (0.4 V vs. Li/Li^+).[3,8,9,11,15] However, promising Si-based materials are also restricted by serious pulverization, electrical contact loss and delamination from current collectors caused by great volume changes (>300%) during lithiation/delithiation processes which lead to severe capacity degradation and poor cycling performance.[1,12,14,16]

To address the challenges above, the moderate oxidization of silicon to form SiO_x ($x \in [0, 2]$) followed by nanosizing its particles could effectively accommodate the strains generated upon lithiation/delithiation and thus buffer the volume changes to prevent their fractures. Despite somewhat capacity decrease by oxidization, SiO_x could still retain theoretical lithium-storage capacities from 2200 to 3580 mAh g^{-1} with much mitigated volume changes of about 200% and extended cycling life, which is therefore taken as the most promising candidates for Si-based anode materials.[17–19] On one side, the poor intrinsic conductivity (6.7×10^{-4} S cm^{-2}) gives rise to the sluggish formation kinetics of Li–O and Li–Si upon charge/discharge which is responsible for large initial irreversible capacity, low initial coulombic efficiency, undoubtedly unfavorable for rate capability. Fortunately, on the other side, LiO_2 could form on the periphery of Si-based particles to construct stable solid electrolyte interfaces (SEI) and buffer the volumetric changes, which should be favorable for cycling performance.[19–21] Therefore, nanostructuring and construction of protective layers are expected to be capable of improving rate capability of and prolonging cycle lifetime of SiO_x anodes

[a] Dr. L. Song, T. Zhao, X. Tan, D. Mao, S. Su, Z. Fan, Prof. W. Chu
Nanofabrication Laboratory, CAS Key Laboratory for Nanomaterials and Photonic Devices
CAS Key Laboratory for Nanosystems and Hierarchical Fabrication
CAS Center for Excellence in Nanoscience
National Center for Nanoscience and Technology
Beijing, 100190, China
E-mail: wgchu@nanoctr.cn
[b] T. Zhao, X. Tan, D. Mao, S. Su, Z. Fan, Prof. W. Chu
Center of Materials Science and Optoelectronics Engineering
University of Chinese Academy of Sciences
Beijing 100049, China

Supporting information for this article is available on the WWW under https://doi.org/10.1002/batt.202100350

© 2022 Wiley-VCH GmbH

Research Article
doi.org/10.1002/batt.202100350

in terms of shortening of Li^+ transport and reaction pathways, stress relaxation and surface protection. SiO_x nanostructures including nanoparticles, nanospheres, nanowires, nanotubes and even various porous two-dimensional structures have been found capable of minimizing the mechanical strains of reactions caused by the volume changes.[22,23] Well-designed protective layers such as carbon-coated, conductive polymers-encapsulated, core-shell and yolk-shell structures enable to not only protect the surfaces but also tolerate the volume variations.[9,15,24] Particularly, novel SiO_x/C composites with internal voids for volume expansions, stable shells for prevention of electrolyte infiltration and erosion, and high conductive carbon-based materials for improvement of electrical conductivity have been well demonstrated using nanostructuring technologies and/or carbon surface-coating strategies.[25] In the past decades, almost all the SiO_x/C anodes suffered from the severe experimental conditions, such as extra addition and/or high temperature pyrolysis of silane precursors and laser ablation of bulk Si, which inevitably obstructs the rapid development of Si-based anodes due to the increase in complexity of materials preparation, energy consumption and cost.[26] Therefore, facile preparation of SiO_x/C anode composites which can simultaneously realize homogenization, nanostructuring and heteroatoms doping is quite intriguing for their applications in LIBs.[8,27]

In this report, willow catkins with abundant surface functional groups and high silicon percentages of about 5–20 wt% normally causing uncomfortable respiratory allergy and air pollution in spring, were used as raw, economical and adequate resources for Si and C-dominated materials (Figure S1a). As intrinsic 1D uniform hollow microtubes, we employed inherent Si and P species in catkins to successfully prepare nitrogen (N) and phosphorus (P) co-decoped SiO_x/carbon (C) nanosheets (N/P-SiO_x/C-NSs) by a urea- and potassium hydroxide-assisted high-temperature treatment strategy. As a result, catkins-derived N/P-SiO_x/C-NSs composites were endowed with high electronic conductivity, robust structure and superior surface/interface stability simultaneously and thus exhibited a reversible capacity as high as 1869.88 mAh g^{-1} at 0.05 A g^{-1}, excellent rate capability and long-term high-rate cycling stability, which are very promising as anode materials for LIBs.

Results and Discussion

The typical preparation procedure of N/P-SiO_x/C-NSs is illustrated in Figure 1. Briefly, the willow catkins composed of microtubes, as shown in Figure S1(a) were washed with acetone and deionized water, and then were supersonicated in ethanol for removing seeds. Subsequently, the cleaned catkins along with potassium hydroxide (KOH) at various ratios were poured into ethanol and heated until the full evaporation of ethanol. The remnant mixtures were pyrolyzed at 400 °C for 3 h and then 850 °C for 1 h in a tubular furnace under argon atmosphere. The KOH was molten for activation to act as scissors which exfoliated and fragmented microtubes into nanosheets. The products thus obtained were mixed with HNO_3 for subsequently hydrothermal treatment at 120 °C for 3 h, which serves to modify abundant active groups on the surface of KOH-catkins. The nanosheets were washed by DI water several times followed by vacuum drying. Finally, the KOH-catkins were mixed with moderate urea ($CO(NH_2)_2$) for nitrogen doping by pyrolyzing at the temperatures ranging from 800 °C to 1000 °C for 1–5 h, which resulted in different N/P-SiO_x/C-NSs. The morphologies of N/P-SiO_x/C-NSs treated with different KOH ratios were shown in Figure S2. No obvious morphological differences were observed for the as-prepared nanosheets with different KOH ratios (KOH:C = 0.5:1, 1:1, and 2:1), accompanied by the formation of similar cross-linked nanosheets and abundant pores at both the inner and outer surfaces of nanosheets. The mass losses of catkins after KOH treatment were about 86% for KOH:C = 0.5:1, 90% for KOH:C = 1:1, and 92% for KOH:C = 2:1. Thus, we chose the samples with KOH:C = 0.5:1 for the targets unless otherwise stated. Figure S3 shows the Fourier Transform Infrared (FT-IR) spectra of KOH-catkins with and without HNO_3 treatments which are quite different, implying the formation of very different surface functional groups after HNO_3 treatments. The peaks around 900–1600 cm^{-1} and 2600–3500 cm^{-1} could be assigned to the

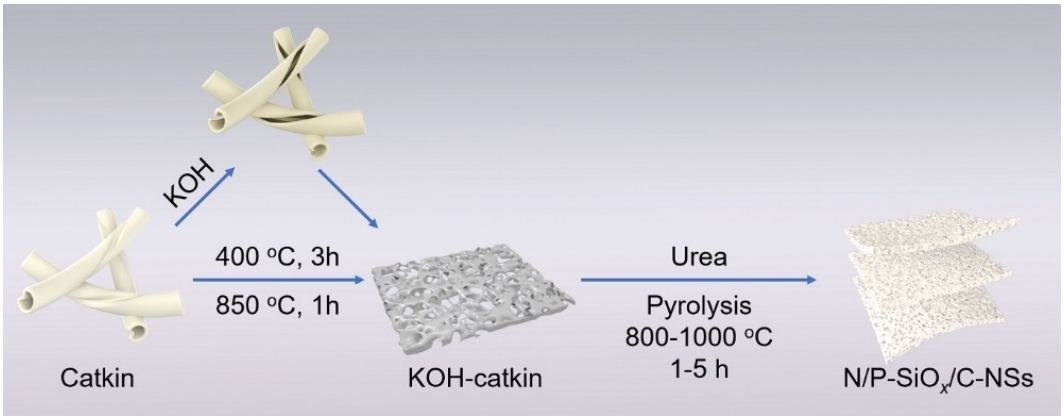

Figure 1. Schematic of the preparation processes of the N/P -SiO_x/C-NSs.

© 2022 Wiley-VCH GmbH

25666223, 2022, 4, Downloaded from https://chemistry-europe.onlinelibrary.wiley.com/doi/10.1002/batt.202100350 by University of Ulsan, Wiley Online Library on [11/11/2025]. See the Terms and Conditions (https://onlinelibrary.wiley.com/terms-and-conditions) on Wiley Online Library for rules of use; OA articles are governed by the applicable Creative Commons License

bending and stretching vibrations of C–OH, respectively,[28] which would be expected to facilitate the subsequent nitrogen doping. Detailly, the peaks around 1000–1100 cm^{-1} could be attribute to Si–O–C absorption peaks. Small δ_{-CH3} and δ_{-CH2} and δ_{-CH} bending vibrations could be clearly observed 1380–1370, ~1465 and ~1340 cm^{-1}, respectively. The peaks between 1250–1000 cm^{-1} and 1500–1300 cm^{-1} could be confirmed the existence of stretching vibrations $\upsilon_{C=O}$ and bending vibrations δ_{-OH}. The obvious peak between 1200–1300 cm^{-1} could be attributed to Si-containing phases. Transmission electron microscopy (TEM) and High-resolution TEM (HRTEM) images of N/P-SiO_x/C-NSs-800-5h, N/P-SiO_x/C-NSs-900-5h and N/P-SiO_x/C-NSs-1000-5h derived with urea treatments at 800, 900 and 1000 °C for 5h, respectively, are displayed in Figures 2(a) and S4 in which randomly orientated nanosheets with fine junction structures can be easily seen. The layered structures of pore walls were revealed by HRTEM (Figure 2b) as well with an interlayer spacing of about 0.348 nm, corresponding to the (002) planes of graphitic carbon (inset of Figure 2b).[15,24]

Nitrogen (N_2) sorption measurements were conducted to identify the porous structures of the catkins and activated N/P-SiO_x/C-NSs-900-5h. The Brunauer-Emmett-Teller (BET) surface areas, pore volumes, and pore size distributions were presented in Figure S5. The N_2 adsorption isotherms of the as-prepared samples were shown in Figure S5(a). A hysteresis loop (type IV) could be easily observed in the activated samples, which indicated that microporous structures had been generated during the KOH activation and urea treatment. With the increasing of KOH activation duration, the surface areas of the catkins and N/P-SiO_x/C-NSs-900-5h could be dramatically increased from 62.5 to 583.58 $m^2 g^{-1}$. The pore size distributions were shown in Figure S5(b and c), where the t-plot curves further confirmed the existence of microporous structures in the activated samples. Such high specific surface areas and ideal microporous structures were desired for the as-prepared nanosheets, which determined the outstanding transport properties of Li ions storage.[11,12]

X-ray diffraction (XRD) patterns of all the samples shown in Figure 2(c) revealed the humps around 22° resulting from the amorphous carbon matrix in the composites, as also indicated by HRTEM in Figure 2(b). One weak peak around 26.5° could be assigned to graphitic carbon (Hexagonal, $P6_3mmc$). The other peaks could be indexed as the mixed crystalline structures similar to tridymite-M O–Si–O (JCPDF#27-0605) and cristobalite O–Si–O (JCPDF#18-1107).[8,29] These structural models were adopted to perform Rietveld refinements on the XRD data of N/P-SiO_x/C-NSs-900-5h, which could basically describe its crystalline structure, as shown in Figure S6. The above structural models based on the Tridymite-M, Cristobalite SiO_x and graphite phases contain $P41\ 1\ 2$, $C1\ C\ 1$, $P3_2\ 2\ 1$, $P31\ 2\ 1$ and $P6_3m\ m\ c$, respectively.[30] Furthermore, elemental mappings by energy dispersive of X-ray (EDS) clearly revealed the homogeneous distributions of C, P, Si, N and O across N/P-SiO_x/C-NSs without the presence of nanoparticles, as shown in Figure 2(d). The Raman spectra further revealed the D bands at round 1350 cm^{-1} and the G bands at about 1590 cm^{-1} for all the samples, suggestive of the presence of both disordered and ordered carbon, as seen in Figure S7. The intensity ratios of G to D band (I_D/I_G) imply different graphitization degrees in the order of N/P-SiO_x/C-NSs-800-5h (0.885) < N/P-SiO_x/C-NSs-1000-5h (0.938) < N/P-SiO_x/C-NSs-900-5h (0.945).[31] The strong and wide peak located at 1100 cm^{-1} for N/P-SiO_x/C-NSs-900-5h and N/P-SiO_x/C-NSs-1000-5h could be assigned to the typical transverse acoustic and transverse optical vibration modes of amorphous Si.[15,32]

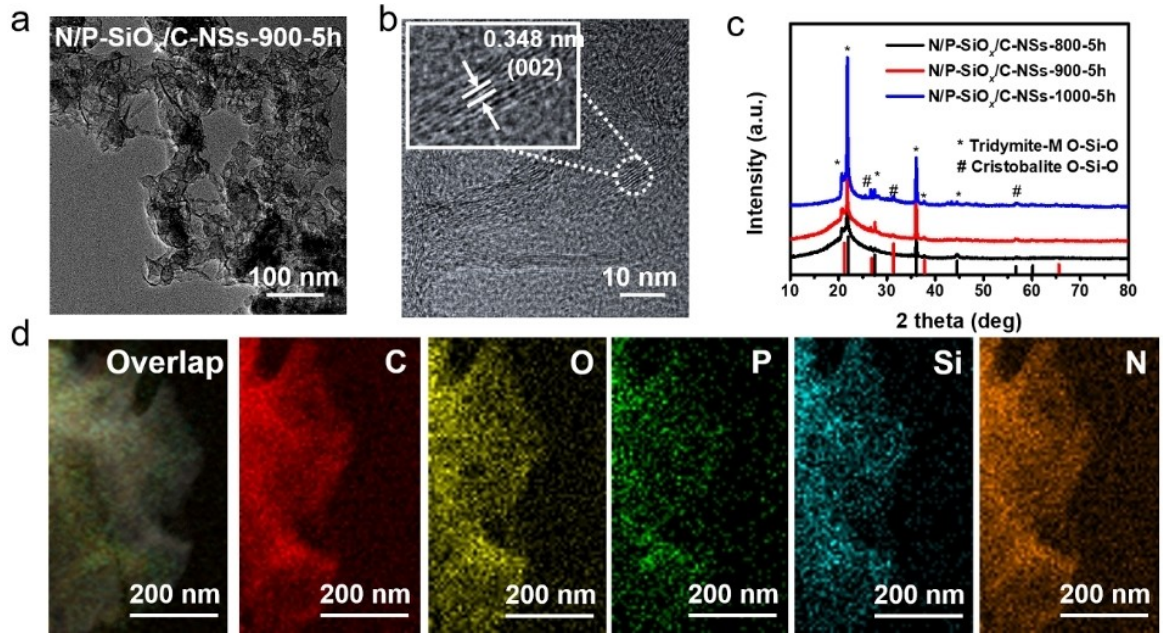

Figure 2. a) TEM and b) HRTEM images of N/P-SiO_x/C-NSs-900-5h. c) XRD patterns of N/P-SiO_x/C-NSs-800-5h, N/P-SiO_x/C-NSs-900-5h and N/P-SiO_x/C-NSs-1000-5h. d) Element mappings of N/P-SiO_x/C-NSs-900-5h.

© 2022 Wiley-VCH GmbH

25666223, 2022, 4, Downloaded from https://chemistry-europe.onlinelibrary.wiley.com/doi/10.1002/batt.202100350 by University of Ulsan, Wiley Online Library on [11/11/2025]. See the Terms and Conditions (https://onlinelibrary.wiley.com/terms-and-conditions) on Wiley Online Library for rules of use; OA articles are governed by the applicable Creative Commons License

Research Article
doi.org/10.1002/batt.202100350
Chemistry Europe
European Chemical Societies Publishing

X-ray photoelectron spectra (XPS) were acquired for analysis of chemical compositions of the samples above, as given in Figure 3. The XPS survey spectra was shown in Figure 3(a), which all confirmed the existence of C, N, O, P and Si and the elemental content analysis were listed in Table S1, indicated that the Si contents were increased to 9.88%, 15.44% and 20.94%, whereas the P and N contents were declined to 8.06%, 1.08%, 0.88% and 1.22%, 1.92%, 1.67% for N/P-SiO_x/C-NSs-800-5h, N/P-SiO_x/C-NSs-900-5h and N/P-SiO_x/C-NSs-1000-5h, which meant the temperature build-up would influence the abundant Si phases and finally affected the Li-ion anode performance. With the increased treatment temperatures, the Si and O percentages increased whereas the P, N and C percentages dropped. It could be easily understood that the increase in treatment temperature could lead to the sizable loss of carbon and nitrogen and thus the change of relative percentages with their crystal structures retained roughly. For N/P-SiO_x/C-NSs-900-5h and N/P-SiO_x/C-NSs-1000-5h, carbon, silicon and oxygen dominate while the relative percentages of nitrogen and phosphorus are only around 1 wt% which could be taken as trace doping. The changes in relative percentages are reasonably expected to influence their electrochemical performance as anodes. The high-resolution N 1s, O 1s, Si 2p, C 1s and P 2p spectra are shown in Figure 3(b–f). For N 1s, four different components at 398.6, 400.0, 401.3 and 405.8 eV could be attributed to pyridinic-N, pyrrolic-N graphitic-N, and oxide-N, respectively. Both pyrrolic-N and pyridinic-N are believed to reside preferentially at the edges which are bonded to the carbon matrix.[7,28] The presence of Si–O_x bonds was further confirmed by high-resolution Si 2p spectra. The deconvoluted components around 101.68, 102.09, 102.54 and 103.03 eV revealed the co-existence of multivalent silicon such as Si^{+}, $SiO_{1.5}$ (Si^{3+}), $SiO_{2.0}C_{2.0}$ and $SiO_{2.0}$ (Si^{4+}).[19,21] For N/P-SiO_x/C-NSs-1000-5h, the relative percentages of Si^{+}, $SiO_{1.5}$ (Si^{3+}), $SiO_{2.0}C_{2.0}$ and $SiO_{2.0}$ (Si^{4+}) components are estimated to be 18.7%, 31.82%, 33.71% and 15.8%, respectively. The typical peaks of Si–O (532.8 eV) and O–Si–O (532.2 eV) were also confirmed by the O 1s spectra (Figure 3d).[18,33] Thus, strong interfacial Si–O bonds would not only enhance the interactions between carbon and SiO_x matrix but also strengthen the nanosheet structure as a conductive framework to increase the electrical conductivity, which would be favorable for the performance. The C 1s spectrum could also be fitted as three components at 288.5, 285.59 and 284.62 eV, respectively, in which the peaks around 285.59 and 284.62 eV could be ascribed to sp^2 hybridized carbon C=C/C–C and ethylene carbon, respectively, and the component at 288.5 eV should be attributed to C–O and O–C=O bonds.[28] The P 2p spectrum could be deconvoluted into three peaks at 132.4, 133.4 and 134.2 eV, which correspond to C–P/C2–P, C3–P and C–O–P groups, respectively.[27,34] Thermogravimetric (TG) curves in air were further taken to estimate the amount of carbon and Si involved in both catkin and N/P-SiO_x/C-NSs-900-5h (Figure S8). For N/P-SiO_x/C-NSs-900-5h, an obvious weight loss from 180 °C to 220 °C could be attributed to the evaporation of the adsorbed organics and/or super polymers at the surfaces and interfaces.[12,19,35] Above 470 °C, the almost unchanged TG curve was observed, suggesting the complete decomposition of carbon and the SiO_x remanants of about 89 wt%. For the catkin precursors, the weight loss is over 85% from 100 °C to 600 °C, indicating the full removal of carbonaceous components and organics and the retaining of remanent inorganic silicon phases over 600 °C.

Here, N/P-SiO_x/C-NSs-800-5h, N/P-SiO_x/C-NSs-900-5h and N/P-SiO_x/C-NSs-1000-5h were paired with Li to form half-cells for tests of electrochemical performance, as shown in Figure 4.[36,37] All the samples exhibit quite impressive high-rate discharge performances at the rates ranging from 0.05 to 10.0 A g^{-1} with their specific capacities listed in Table S2. N/P-SiO_x/C-NSs-900-5h shows the attractivecapacities of 1869.88 mAh g^{-1}

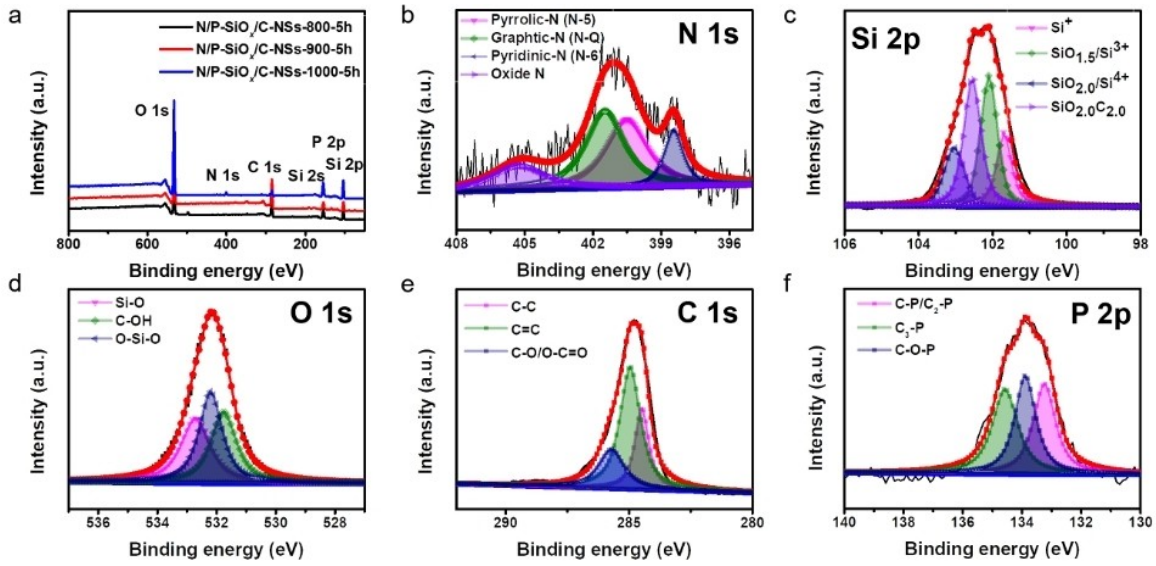

Figure 3. a) XPS survey spectra of N/P-SiO_x/C-NSs-800-5h, N/P-SiO_x/C-NSs-900-5h and N/P-SiO_x/C-NSs-1000-5h. b–f) High-resolution N 1s, Si 2p, O 1s, C 1s and P 2p spectra of N/P-SiO_x/C-NSs-900-5h.

© 2022 Wiley-VCH GmbH

25666223, 2022, 4, Downloaded from https://chemistry-europe.onlinelibrary.wiley.com/doi/10.1002/batt.202100350 by University of Ulsan, Wiley Online Library on [11/11/2025]. See the Terms and Conditions (https://onlinelibrary.wiley.com/terms-and-conditions) on Wiley Online Library for rules of use; OA articles are governed by the applicable Creative Commons License

Research Article
doi.org/10.1002/batt.202100350
Chemistry Europe
European Chemical Societies Publishing

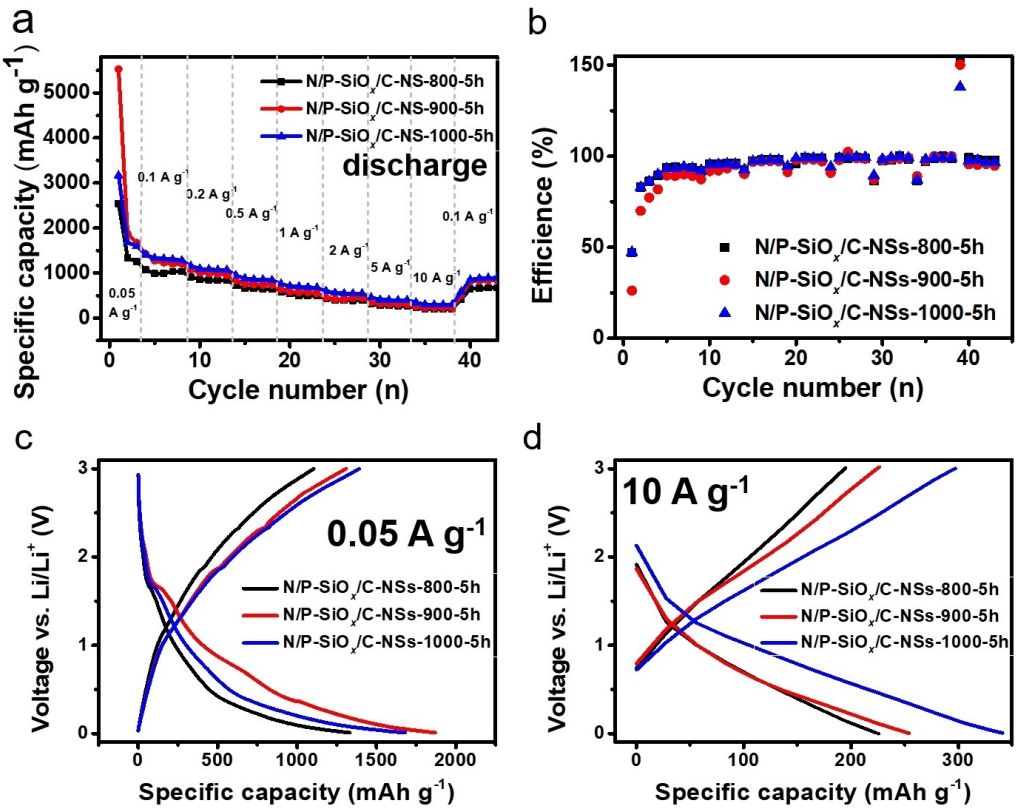

Figure 4. Electrochemical performances of N/P-SiO_x/C-NSs-800-5h, N/P-SiO_x/C-NSs-900-5h and N/P-SiO_x/C-NSs-1000-5h in Li-half cells. a, b) Cycling performances and Coulombic efficiencies at various current densities gradually increasing from 0.05 to 10 A g^{-1}. c, d) GDC profiles at 0.05 and 10 A6 g^{-1}. The gravimetric specific capacities were calculated on the basis of the mass of the N/P-SiO_x/C-NSs in the electrodes.

(0.05 A g^{-1}) and 1418.26 mAh g^{-1} (0.1 A g^{-1}) at low current densityand the impressivecapacity of 254.29 mAh g^{-1} (10.0 A g^{-1}) at high current density, whereas N/P-SiO_x/C-NSs-1000-5h shows the lower capacity of 1679.79 mAh g^{-1} (0.05 A g^{-1}) at low current densitys and the higher capacity of 341.34 mAh g^{-1} (10.0 A g^{-1}) at high current density. Their superior rate capability of N/P-SiO_x/C-NSs could be attributed to the efficient electrical conduction arising from the unique structures, the graphitized carbon and the homogenous doping of heteroatoms into the SiO_x/C-NSs composites. In particular, the higher capacities achieved for N/P-SiO_x/C-NSs-1000-5h at higher current density might be related to the better electronic conduction caused by the presence of the higher graphitized carbon at higher temperature. The N/P-SiO_x/C-NSs anodes displayed unprecedentedly high gravimetric specific capacities of 2538.304, 5525.654 and 3167.793 mAh g^{-1} upon first discharge, respectively and then corresponding reversible capacities of 1331.49, 1869.88 and 1679.79 mAh g^{-1} for next cycle, as shown in Table S1, which presented relatively low initial coulombic efficiencies (ICE) of 52.46%, 33.84% and 53%, respectively, followed by the achievement of reversible columbic efficiencies (RCE) between 97% and 99% due to their superior cycling stability, as revealed in Figure 4(b). To reveal the electrochemical properties, the cyclic voltammetry (CV) curves of N/P-SiO_x/C-NSs-900-5h at a sweep rate of 0.1 mV s^{-1} with a voltage window of 0.01–3 V for initial three cycles are shown in Figure S9. The largest irreversible peak around 1.267 V present in the first two cycles implied the formation of a solid electrolyte interface (SEI). The irreversible strong peak at below 0.05 V suggested the lithiation and delithiation in the Si–O–C units, while the Li insertion into graphitized carbon due to the formation of diversified defects of 2D architectures, layers, pores and cavities. Within these, Li atoms would bind with heteroatoms located at the boundaries formed among differently oriented graphite crystallites. The peaks below 0.5 V are associated with lithium metal under potential deposition.[18,34] More active sites such as defects and vacancies for Li storage were generated by self-doping of phosphorus into and doping of alien nitrogen into the SiO_x/C nanosheet composites.[22,33] A broad distribution of adequate active sites for Li storage is believed to be favorable for the performance of this type of SiO_x/C composites, as already shown above.[21,38]

The initial rapid capacity fade signals the formation of SEI on the carbon component in the SiO_x/C composites, as confirmed by the vanishing discharge plateau of 0.9–0.8 V at 0.05 A g^{-1} shown in Figures 4(c and d) and S10.[36] A broad and inclined discharge platform is observed below 0.5 V which may result from an interfacial intercalation of Li^+ into the micro/nano-pores in the SiO_x/C composites and a further probable insertion of Li^+ into the interlayers of nanosheets. The subsequent galvanostatic discharge-charge (GDC) profiles become similar with the capacities predominantly from the discharge within the low-voltage range, which is beneficial to the improvement of energy density of a battery on one side

© 2022 Wiley-VCH GmbH

25666223, 2022, 4, Downloaded from https://chemistry-europe.onlinelibrary.wiley.com/doi/10.1002/batt.202100350 by University of Ulsan, Wiley Online Library on [11/11/2025]. See the Terms and Conditions (https://onlinelibrary.wiley.com/terms-and-conditions) on Wiley Online Library for rules of use; OA articles are governed by the applicable Creative Commons License

Research Article
doi.org/10.1002/batt.202100350
Chemistry Europe
European Chemical Societies Publishing

(Figure S10a–c). On the other side, the nanosheet structures with rich micro/nano-pores could not only provide an adequate electrode/electrolyte contact area but also offer sufficient channels of Li^+ transport, which undoubtedly leads to superior kinetics of Li^+ insertion/deinsertion during the discharge-charge processes, as evidenced by their outstanding rate performances at high current densities (Figure 4a). To assess the cycling stability, cycle performances of N/P-SiO_x/C-NSs-900-5h at 10 and 0.1 A g^{-1} along with their discharge/charge curves at different cycling numbers are shown in Figure 5. For the rate as high as 10 A g^{-1} (Figure 5a and c), both the charge and discharge capacities increased firstly within 1200 cycles, and then tended to decrease slightly and level off. After 10000 cycles, a discharge capacity as high as 311 mAh g^{-1} could be still achieved, suggesting the unprecedent high-rate cycling stability. In sharp contrast, for the rate of 0.1 A g^{-1} (Figure 5b and d), the cycling performance tended to decrease slightly for 60 cycles. The N/P-SiO_x/C-NSs-900-5h showed an exceptionally high gravimetric specific capacity of 1392.83 mAh g^{-1} upon discharge and then a reversible charge capacity of 1131.63 mAh g^{-1} in the first cycle, giving a reasonable RCE of 81.25%.

By further treating with urea N/P-SiO_x/C-NSs-900 for extra 1 h and 3 h to optimize the pyrolysis durations, both the rate performances were deteriorated, as clearly revealed in Figure S11. In addition, we treated N/P-SiO_x/C-NSs-900-5h at 900 °C for 12 h in air in order to remove the carbon and retain the silicon with the unchanged valences as possible, as shown in the XRD pattern (Figure S12a). The samples thus treated showed very poor rate performance, as shown in Figure S12(b), which confirmed the crucial role of carbon in performance. Furthermore, HF treatment could be used to remove the SiO_x in the N/P-SiO_x/CNSs-900-5h (denoted as N/P-CNSs-900-5h) (Figure S13a), which the capacity of carbon can be determined. As shown in Figure S13(b), the N/P–CNSs-900-5h displayed only 356 mAh g^{-1} under 0.05 A g^{-1}.

To demonstrate the scalability of our materials and electrode preparation, Figure S13 displays the rate and cycling performances of N/P-SiO_x/C-NSs-900-5h coated on Cu foil followed by calendaring to achieve an industrial loading level of active mass (ca. 2.0 mg cm^{-2}). The reversible capacity was 356.09, 269.8373, 216.87, 168.88, 128.82, 100.56, 76.38 and 58.30 mAh g^{-1} for 0.05, 0.1, 0.2, 0.5, 1, 2, 5 and 10 A g^{-1}, respectively. At 0.1 A g^{-1}, 1000 cycles led to a capacity of 175.13 mAh g^{-1} which gives a capacity decay rate of 0.08 mAh g^{-1} per cycle, as shown in Figure S14(d). When the current density increased to 10 A g^{-1}, the capacity of N/P-SiO_x/C-NSs-900-5h could be retained ca. 65 mAh g^{-1}, as shown in Figure S14(e). Compared with the literature, N/P-SiO_x/C-NSs-900-5h displays quite high capacities and superior long-term cycling stability, as seen in Table S3.

To further comprehend the electrochemical kinetics of the N/P-SiO_x/C-NSs-900-5h, N/P-SiO_x/C-NSs-900-5h and N/P-SiO_x/C-NSs-1000-5h electrodes after cycles. CV measurements were carried out at different sweeping rates from 1 to 50 mV s^{-1}.[17,18] As clearly demonstrated in Figure S15(a, c and e), the shape of the CV curves recorded at various scan rates was similar except for a slight peak shift as the sweep rates increase, which demonstrates the exceptional kinetics and weak polarization of the electrodes at high scan rates. To further probe the pseudocapacitive contribution at various sweeping speeds, the calculation can be carried out by the following equation:

$$\log(i) = \log a + b\log v$$

where a and b are two adjustable constants, i and v are assigned to the peak current (mA) and the scan rate (mV s^{-1}). The b value obtained from the slope of the log(i)-log$v$ fitted line is used to identify the storage mechanism. In general, the b value approaching 0.5 demonstrates the diffusion-controlled reaction and when the b value is equal to 1, the reaction is conducted with a pseudocapacitive Li-ion storage

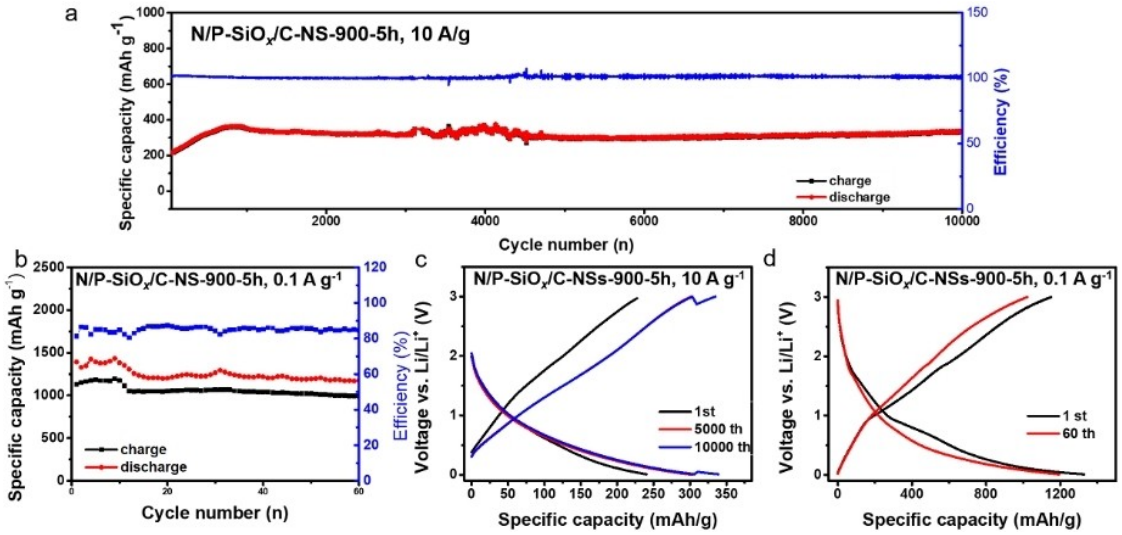

Figure 5. a, b) Cycling performance and RCE plots of N/P-SiO_x/C-NSs-900-5h at 10 and 0.1 A g^{-1}. Voltage profiles of c) 1st, 5000th and 10000th at a current density of 10 A g^{-1}, and d) 1st and 60th at a current density of 0.1 A g^{-1}.

© 2022 Wiley-VCH GmbH

25666223, 2022, 4, Downloaded from https://chemistry-europe.onlinelibrary.wiley.com/doi/10.1002/batt.202100350 by University of Ulsan, Wiley Online Library on [11/11/2025]. See the Terms and Conditions (https://onlinelibrary.wiley.com/terms-and-conditions) on Wiley Online Library for rules of use; OA articles are governed by the applicable Creative Commons License

Research Article
doi.org/10.1002/batt.202100350

mechanism.[4–6,8] If the value is in the range of 0.5–1, the process is jointly controlled by diffusion and capacitance. A favorable linear relationship could be observed for N/P-SiO_x/C-NSs-900-5h, N/P-SiO_x/C-NSs-900-5h and N/P-SiO_x/C-NSs-1000-5h electrodes,[7] as shown in Figure S15(b, d and f), the calculated *b* values of N/P-SiO_x/C-NSs-900-5h, N/P-SiO_x/C-NSs-900-5h and N/P-SiO_x/C-NSs-1000-5h are 0.32, 0.51 and 0.47, respectively, i indicating the major contribution from the diffusion-controlled reactions.

To demonstrate the structural durability of N/P-SiO_x/C-NSs-900-5h, we employed observe the morphological evolution SEM and XRD tests to determine the morphologies and phases of N/P-SiO_x/C-NSs-900-5h after 10000 cycles (Figure S16a and b). After 10000 cycles, the visible 3D nanosheets structures and voids could still observe in N/P-SiO_x/C-NSs-900-5h (Figure S16a), whereas O–Si–O phases were stable after cycles compared with N/P-SiO_x/C-NSs-900-5h. Figure S17 displayed the elemental mapping of N/P-SiO_x/C-NSs-900-5h after 10000 cycles, the C, O, N, P and Si were stable and homogeneously distributed in the anode materials. Notably, the amount of F could be attributed to the binder PVDF or electrolyte decomposition.[5,16] In addition, charge-transfer resistance (R_{ct}) and structural stability of N/P-SiO_x/C-NSs-900-5h were evaluated by using electrochemical impedance spectroscopy analysis and examining morphology changes after lithiation/delithiation cycling.[3,6] Figure S18 describes the Nyquist plots of the N/P-SiO_x/C-NSs-900-5h before and after cycles. The diameter of the semicircle e at the high-frequency regions of N/P-SiO_x/C-NSs-900-5h is smaller than that of N/P-SiO_x/C-NSs-900-5h after 10000 cycles, which meant the increase of R_{ct} (62 and 83 Ω, respectively) after cycling. Furthermore, the CV curve at a sweep rate of 0.1 mV s^{-1} with a voltage window of 0.01–3 V of N/P-SiO_x/C-NSs-900-5h after 10000 cycles was shown in Figure S19, the strong peak at below 0.05 and 0.5 V kept stable which meant the lithiation and delithiation in the Si–O–C units and lithium metal under potential deposition, as the same as N/P-SiO_x/C-NSs-900-5h. Consequently, the structures could be stable after 10000 cycles.

Conclusion

In conclusion, we prepared successfully hierarchically porous nitrogen and phosphorus heteroatoms co-doped SiO_x/C composite nanosheet architectures (N/P-SiO_x/C-NSs) from environmentally unfriendly catkins without the introduction of alien silicon. The microtube-structured catkins were fully converted to nanosheets by using KOH as both scissors and activation agents. This unique architecture comprised of novel multiphase composites ensures fast kinetics of ion transport and excellent electrical conduction, and formation of rigid frameworks, accompanied by the supply of sufficient Li^+ storage sites as Li^+ reservoir. This, along with the heteroatom doping of nitrogen and phosphorus led to outstanding rate capability and long-term high-rate cycling stability as anodes for lithium-ion batteries. N/P-SiO_x/C-NSs-900-5h delivered the capacities over 1300 mAh g^{-1} at low current densities and showed almost no capacity fade over 10000 cycles at a rate as high as 10 A g^{-1}. Different treatment recipes resulted in differing electrochemical performances, which could be ascribed to their different relative percentages of SiO_x, carbon, oxygen, nitrogen and phosphorus despite the retaining of the similar crystal structures. The present study provides a novel strategy for preparing high performance energy storage or conversion materials from biomass materials using inorganics instead of organic carbon involved as sources through chemical exfoliation and treatments.

Experimental Section

All the chemicals were of analytical grade and commercially available from Shanghai Chemical Reagent Co., Ltd and were used without further purification.

Preparation of N/P-SiO_x/C-NSs anode materials

The catkins were collected randomly, and washed by double distilled water and acetone for several times to get rid of seeds and dusts. The white, cotton-like, mechanical-resilience catkins thus treated were mixed with potassium hydroxide (KOH) (C:KOH = 0.5:1, 1:1, 2:1) using ethanol as solvent, which were dired by heating. The dried mixture was pyrolyzed in a tubular furnace at 400 °C for 3 h and then 850 °C for 1 h with a heating rate of 5 °C min^{-1} under argon atmosphere, and further subject to hydrothermal treatment for activation in 3 M HNO_3 at 120 °C for 3 h. The products thus obtained were washed several times using deionized water until pH = 7 which were then vacuum dried and collected as KOH-catkins. Finally, the mixture of KOH-catkins was mixed with proper amount of urea ($CO(NH_2)_2$) (urea:C = 2:1) as nitrogen sources and pyrolyzed at 800 °C, 900 °C and 1000 °C for 5 h in argon atmosphere to achieve N/P-SiO_x/C-NSs-800-5h, N/P-SiO_x/C-NSs-900-5h and N/P-SiO_x/C-NSs-1000-5h, respectively.

Preparation of carbon-free SiO_x-based materials

To explore the role of carbon in N/P-SiO_x/C-NSs-900-5h, further pyrolysis at 900 °C for 12 h at a heating rate of 5 °C min^{-1} in a tubular furnace in air was performed to remove the carbon with the valences of silicon unchanged as possible for the achievement of carbon-free SiO_x-based materials.

Characterization

Scanning electron microscopy (SEM) and energy filtered scanning electron microscopy (EFSEM) observations were performed on a Hitachi SU8200 microscope operated at an acceleration voltage of 5 kV. High-resolution Transmission electron microscopy (HRTEM) images and selected-area electron diffraction (SAED) patterns were acquired on a Tecnai G2 F20U-TWIN microscope operated at an accelerating voltage of 200 kV. X-ray photoelectron spectra (XPS) were acquired on a ThermoFisher Scientific ESCALab 250Xi spectrometer with 300 W monochromatic Al K_α radiation. Raman spectroscopy measurements were performed on a Renishaw in Via plus spectrometer with a 532 nm laser for characterization of graphitic and amorphous carbon and other bonds. Fourier transform infrared (FTIR) spectra were recorded on a PerkinElmer Spectrum One spectrometer within a scan range from 4000 to 500 cm^{-1} at room temperature.

© 2022 Wiley-VCH GmbH

25666223, 2022, 4, Downloaded from https://chemistry-europe.onlinelibrary.wiley.com/doi/10.1002/batt.202100350 by University of Ulsan, Wiley Online Library on [11/11/2025]. See the Terms and Conditions (https://onlinelibrary.wiley.com/terms-and-conditions) on Wiley Online Library for rules of use; OA articles are governed by the applicable Creative Commons License

25666223, 2022, 4, Downloaded from https://chemistry-europe.onlinelibrary.wiley.com/doi/10.1002/batt.202100350 by University of Ulsan, Wiley Online Library on [11/11/2025]. See the Terms and Conditions (https://onlinelibrary.wiley.com/terms-and-conditions) on Wiley Online Library for rules of use; OA articles are governed by the applicable Creative Commons License

Electrochemical tests

Electrochemical tests were carried out using CR2025 coin-type cells. The active material, acetylene black, and polyvinylidenefluride (PVDF) were ground at a ratio of 8:1:1 in N-methyl-2-pyrrolidone (NMP) and then coated uniformly on copper foils and dried in a vacuum oven at 80 °C for 12 h. The above foils were cut into discs with a radius of 0.785 cm as working electrodes, followed by pressing under 20 MPa for 15–20 s. The cells were assembled in an argon-filled glove box ($H_2O < 0.1$ ppm, and $O_2 < 0.1$ ppm) with a lithium-metal counter electrode and Celgard separator. The electrolyte was 1 M LiPF6 dissolved in a mixture of ethylene carbonate (EC), ethyl methyl carbonate (EMC) and dimethyl carbonate (DMC) in a volume ratio of 1:1:1. Electrochemical performances were tested on a battery test system (Neware Company, China) at room temperature (around 25 °C). Cyclic voltammetry (CV) and electrochemical impedance spectroscopy (EIS) measurements were carried out on the electrochemical workstation (CHI660D, Shanghai Chenhua Company, China).

Acknowledgements

We acknowledge the funding support from the National Natural Science Foundation of China under grant No. 51802054, No. 202M680476 and Strategic Priority Research Program of the Chinese Academy of Sciences, grant No. Y9F3XD01ZX.

Conflict of Interest

The authors declare no conflict of interest.

Data Availability Statement

The data that support the findings of this study are available in the supplementary material of this article.

Keywords: anodes of Li-ion batteries · biomass-derived SiO_x/carbon nanomaterials · heteroatoms doped SiO_x/carbon architectures · lithium-ions storage · ultra-long cycle performance

[1] B. Chen, L. Zu, Y. Liu, R. Meng, Y. Feng, C. Peng, F. Zhu, T. Hao, J. Ru, Y. Wang, J. Yang, *Angew. Chem. Int. Ed.* **2020**, *59*, 3137–3142; *Angew. Chem.* **2020**, *132*, 3161–3166.
[2] Y. Zhang, Z. Mu, J. Lai, Y. Chao, Y. Yang, P. Zhou, Y. Li, W. Yang, Z. Xia, S. Guo, *ACS Nano* **2019**, *13*, 2167–2175.
[3] C. Jo, A. S. Groombridge, J. De La Verpilliere, J. T. Lee, Y. Son, H.-L. Liang, A. M. Boies, M. De Volder, *ACS Nano* **2020**, *14*, 698–707.
[4] J. L. Shi, D. D. Xiao, M. Ge, X. Yu, Y. Chu, X. Huang, X. D. Zhang, Y. X. Yin, X. Q. Yang, Y. G. Guo, L. Gu, L. J. Wan, *Adv. Mater.* **2018**, *30*, 1705575–1705581.
[5] X. Wu, Y. L. Chen, Z. Xing, C. W. K. Lam, S. S. Pang, W. Zhang, Z. C. Ju, *Adv. Energy Mater.* **2019**, *9*, 1900343–1900351.
[6] G. R. Yang, P. R. Ilango, S. L. Wang, M. S. Nasir, L. L. Li, D. X. Ji, Y. X. Hu, S. Ramakrishna, W. Yan, S. J. Peng, *Small* **2019**, *15*, 1900628–1900635.
[7] Y. L. Zhang, Z. J. Mu, J. P. Lai, Y. G. Chao, Y. Yang, P. Zhou, Y. J. Li, W. X. Yang, Z. H. Xia, S. J. Guo, *ACS Nano* **2019**, *13*, 2167–2175.
[8] W. Zhang, Y. Weng, W. Shen, R. Lv, F. Kang, Z.-H. Huang, *Carbon* **2020**, *158*, 163–171.
[9] H. Xu, Y. Wang, R. Chen, Y. Bai, T. Li, H. Jin, J. Wang, H. Xia, *Carbon* **2020**, *157*, 330–339.
[10] Y. H. Zhang, N. N. Wang, Z. X. Lu, P. Xue, Y. L. Liu, Y. J. Zhai, B. Tang, M. Q. Guo, L. Qin, Z. C. Bai, *Electrochim. Acta* **2019**, *296*, 891–900.
[11] X. Zhou, Y. Liu, Y. Ren, T. Mu, X. Yin, C. Du, H. Huo, X. Cheng, P. Zuo, G. Yin, *Adv. Funct. Mater.* **2021**, *31*, 2101145–2101152.
[12] H. Wu, L. Zheng, N. Du, B. Sun, J. Ma, Y. Jiang, J. Gong, H. Chen, L. Wang, *ACS Appl. Mater. Interfaces* **2021**, *13*, 22323–22331.
[13] Q. Shi, J. Zhou, S. Ullah, X. Yang, K. Tokarska, B. Trzebicka, H. Q. Ta, M. H. Ruemmeli, *Energy Storage Mater.* **2021**, *34*, 735–754.
[14] Z. Yi, Y. Qian, C. Cao, N. Lin, Y. Qian, *Carbon* **2019**, *149*, 664–671.
[15] M. H. Parekh, A. D. Sediako, A. Naseri, M. J. Thomson, V. G. Pol, *Adv. Energy Mater.* **2020**, *10*, 1902799–1902808.
[16] G. Zhu, F. Zhang, X. Li, W. Luo, L. Li, H. Zhang, L. Wang, Y. Wang, W. Jiang, H. K. Liu, S. X. Dou, J. Yang, *Angew. Chem. Int. Ed.* **2019**, *58*, 6669–6673; *Angew. Chem.* **2019**, *131*, 6741–6745.
[17] H. Wang, X. Yang, Q. Wu, Q. Zhang, H. Chen, H. Jing, J. Wang, S.-B. Mi, A. L. Rogach, C. Niu, *ACS Nano* **2018**, *12*, 3406–3416.
[18] G. Shao, D. A. H. Hanaor, J. Wang, D. Kober, S. Li, X. Wang, X. Shen, M. F. Bekheet, A. Gurlo, *ACS Appl. Mater. Interfaces* **2020**, *12*, 46045–46056.
[19] L. Hu, W. Xia, R. Tang, R. Hu, L. Ouyang, T. Sun, H. Wang, *Front. Chem.* **2020**, *8*, 388–395.
[20] X. Du, H. Zhang, X. Lan, B. Yuan, R. Hu, *Energy Environ. Mater.* **2021**, DOI: 10.1002/eem1002.12186.
[21] L. Liu, X. Li, G. He, G. Zhang, G. Su, C. Fang, *J. Alloys Compd.* **2020**, *836*, 155407–155414.
[22] Z. Yang, Y. Du, G. Hou, Y. Ouyang, F. Ding, F. Yuan, *Electrochim. Acta* **2020**, *329*, 135141–135150.
[23] F. Wang, J. Mao, *ACS Appl. Mater. Interfaces* **2021**, *13*, 13191–13199.
[24] H. J. Kwon, J.-Y. Hwang, H.-J. Shin, M.-G. Jeong, K. Y. Chung, Y.-K. Sun, H.-G. Jung, *Nano Lett.* **2020**, *20*, 625–635.
[25] P. Li, J.-Y. Hwang, Y.-K. Sun, *ACS Nano* **2019**, *13*, 2624–2633.
[26] Y. Li, G. Wang, T. Wei, Z. Fan, P. Yan, *Nano Energy* **2016**, *19*, 165–175.
[27] Y.-C. Zhang, Y. You, S. Xin, Y.-X. Yin, J. Zhang, P. Wang, X.-s. Zheng, F.-F. Cao, Y.-G. Guo, *Nano Energy* **2016**, *25*, 120–127.
[28] L.-T. Song, Z.-Y. Wu, H.-W. Liang, F. Zhou, Z.-Y. Yu, L. Xu, Z. Pan, S.-H. Yu, *Nano Energy* **2016**, *19*, 117–127.
[29] Z. Ye, Y. Jiang, T. Feng, Z. Wang, L. Li, F. Wu, R. Chen, *Nano Energy* **2020**, *70*, 104532–104540.
[30] X. Tan, J. Zhao, M. Jiang, S. Nie, Y. Li, X. Wang, Y. Wang, X. Kang, H. Wang, W. Chu, *Ionics* **2021**, *27*, 4249–4257.
[31] L. Zhang, R. Rajagopalan, H. Guo, X. Hu, S. Dou, H. Liu, *Adv. Funct. Mater.* **2016**, *26*, 440–446.
[32] J. Lee, J. Moon, S. A. Han, J. Kim, V. Malgras, Y.-U. Heo, H. Kim, S.-M. Lee, H. K. Liu, S. X. Dou, Y. Yamauchi, M.-S. Park, J. H. Kim, *ACS Nano* **2019**, *13*, 9607–9619; L. Tong, P. Wang, A. Chen, F. Qiu, W. Fang, J. Yang, C. Wang, Y. Yang, *Carbon* **2019**, *153*, 592–601.
[33] E. Sivonxay, M. Aykol, K. A. Persson, *Electrochim. Acta* **2020**, *331*, 135344–135352.
[34] J. H. Hou, C. B. Cao, F. Idrees, X. L. Ma, *ACS Nano* **2015**, *9*, 2556–2564.
[35] D. Chen, C. Tao, T. Chen, X. Liu, Y. Liu, G. Xu, G. Han, *Nanotechnology* **2021**, *32*, 095402–095414.
[36] Z. L. Yu, S. Xin, Y. You, L. Yu, Y. Lin, D. W. Xu, C. Qiao, Z. H. Huang, N. Yang, S. H. Yu, J. B. Goodenough, *J. Am. Chem. Soc.* **2016**, *138*, 14915–14922.
[37] X. Hui, R. Zhao, P. Zhang, C. Li, C. Wang, L. Yin, *Adv. Energy Mater.* **2019**, *9*, 1901065–1901073.
[38] C.-C. Hsieh, Y.-G. Lin, C.-L. Chiang, W.-R. Liu, *Ceram. Int.* **2020**, *46*, 26598–26607.

Manuscript received: November 18, 2021
Revised manuscript received: January 20, 2022
Accepted manuscript online: January 27, 2022
Version of record online: February 9, 2022

© 2022 Wiley-VCH GmbH